Sparsity-Promoting Dynamic Mode Decomposition Applied to Sea Surface Temperature Fields

Zhicheng Zhang[1†], Yoshihiko Susuki[1] and Atsushi Okazaki[2]

[1]Department of Electrical Engineering, Kyoto University, Katsura, Nishikyo-Ku, Kyoto 615-8510, Japan
(E-mail: zhang.zhicheng.2c@kyoto-u.ac.jp; susuki.yoshihiko.5c@kyoto-u.ac.jp)
[2]Institute of Advanced Academic Research, Chiba University, 1-33 Yayoi-cho, Inage, Chiba 263-0022, Japan
(E-mail: atsushi.okazaki@chiba-u.jp)

Abstract: In this paper, we leverage Koopman mode decomposition to analyze the nonlinear and high-dimensional climate systems acting on the observed data space. The dynamics of atmospheric systems are assumed to be equation-free, with the linear evolution of observables derived from measured historical long-term time-series data snapshots, such as monthly sea surface temperature records, to construct a purely data-driven climate dynamics. In particular, sparsity-promoting dynamic mode decomposition is exploited to extract the dominant spatial and temporal modes, which are among the most significant coherent structures underlying climate variability, enabling a more efficient, interpretable, and low-dimensional representation of the system dynamics. We hope that the combined use of Koopman modes and sparsity-promoting techniques will provide insights into the significant climate modes, thus allowing reduced-order modeling of the climate system and offering a potential framework for predicting and controlling weather and climate variability.

Keywords: Koopman mode decomposition, data-driven modeling, sparsity-promoting, model-reduction, SST application

1. INTRODUCTION

Discovering dominant coherent structures with dynamical and physical implications in climate systems, such as intraseasonal and Madden Julian Oscillation, seasonal El Niño and La Niña–Southern Oscillation, and sea surface temperature anomalies [1], is an important issue in Earth's system modeling, estimation, variability, forecasting, and control [2], and remains a primary focus in atmospheric, ocean, and climate science.

However, the dynamics of climate's states evolving in a finite dimensional phase space naturally contain nonlinear trends, including multiple equilibria, bifurcations, strange attractors, turbulence, and riddled basins. On the one hand, these complexities inherently make the limitations of traditional methods, such as the linear inverse model (LIM) [3], in extracting coherent structures and predicting atmospheric processes, especially when it comes to revealing nonlinear behavior. On the other hand, while practical methods such as those based on empirical orthogonal functions (EOFs) [4] can provide valuable insights into the dominant modes of variability in climate systems, they often lack a direct connection to the underlying dynamics.

In recent decades, the operator-theoretic approach, with a focus on the Koopman operator [5], has gained great attention for analyzing dynamical systems by lifting nonlinear dynamics into a linear representation. This state-of-the-art method describes the linear evolution of observables in an infinite-dimensional functional space [6, 7]. Needless to say, applied Koopmanism played a growing role in uncovering structures in (geophysical) fluid dynamics [8, 9] and in interpreting coherent modes in climate and weather systems. When Koopman mode decomposition (KMD) [10] is combined with its numer-

ical counterparts, such as various dynamic mode decomposition (DMD) [11, 12], it provides spectral analysis for decomposing spatiotemporal patterns. Related literature has validated these methods for capturing climate-related phenomena, including the Madden–Julian Oscillation (MJO) [13] and its dominant component, tropical intraseasonal variability [14, 15], the El Niño–Southern Oscillation (ENSO) [16, 17], the sea surface temperature (SST) anomalies [18], the Pacific Decadal Oscillation (PDO) [19], and sea ice cover variability [20]. Notably, Navarra et al. [18] estimated the transfer and Koopman operators based on one-dimensional Niño-3 time series data and monthly mean Pacific SST, where the state density was derived from the transfer or Koopman eigenfunctions. Subsequently, the variability of tropical ocean and PDO of global SST were identified via Koopman modes [19], and examined the continuous spectrum [6, 21].

Building on these results, this paper focuses on the performance and model reduction of KMD applied to real-world, data-driven climate dynamics. More precisely, we examine three distinct time scales associated with different observable spaces: the variability of SST fields on intraseasonal or monthly (high resolution), seasonal (medium resolution), and annual (low resolution) cycles. Notably, our work differs from existing SST studies using kernel methods [18, 19] by taking sparsity-promoting dynamic mode decomposition (SPDMD) [12] method to extract leading modes and illustrate climate variability.

This is accomplished by penalizing an additional ℓ_1-norm in the least-squares error minimization, which promotes sparsity and ensures the selection of the most significant modes with *nonzero amplitudes*, rather than relying on the magnitude of eigenvalues as in standard DMD [11]. One of the benefits of SPDMD is that it can make a trade-off between accuracy (i.e., performance loss with respect to residual error) and model complexity (i.e.,

---

† Zhicheng Zhang is the presenter of this paper.

the number of modes) by tuning the sparsity weights, offering users flexible choices. Moreover, by comparing methods such as DMD and companion-based DMD (CDMD) [8], we demonstrate that SPDMD provides an effective approach for identifying dominant Koopman modes, thereby potentially revealing a low-dimensional climate dynamics from SST data fields [22].

The rest of this paper is organized as follows: Section 2 introduces the DMD method for approximating the KMD, and deriving a low-dimensional linear system via SPDMD. Section 3 presents three experiments on SST data, extracting dominant Koopman modes to analyze spatial and temporal structures in climate systems. Finally, Section 4 concludes the paper.

2. METHODOLOGIES

2.1. Method-I: Dynamic Mode Decomposition

We start by collecting discrete-time snapshots, that is, a finite sequence of data pairs $\{\mathbf{x}_k, \mathbf{T}(\mathbf{x}_k)\}_{k=0}^{N-1}$ satisfying $\mathbf{y}_k = \mathbf{x}_{k+1} = \mathbf{T}(\mathbf{x}_k)$, which can be concisely represented using the following matrices:

$$\mathbf{Y} = \begin{bmatrix} \mathbf{y}_0\, \mathbf{y}_1\, \cdots\, \mathbf{y}_{N-1} \end{bmatrix} \text{ and } \mathbf{Y}^+ = \begin{bmatrix} \mathbf{y}_1\, \mathbf{y}_2\, \cdots\, \mathbf{y}_N \end{bmatrix}, \quad (1)$$

where $\mathbf{Y}, \mathbf{Y}^+ \in \mathbb{R}^{p \times N}$ and typically $p \gg N$. The concept is to interpret the observed data as sampled snapshots of the studied system's process, governed by an unknown dynamics $\mathbf{T}(\cdot)$. From (1), the resultant evolution can be derived by a discrete-time linear time-invariant system

$$\mathbf{y}_{k+1} = \mathbf{A}\mathbf{y}_k, \quad \Longrightarrow \quad \mathbf{Y}^+ = \mathbf{A}\mathbf{Y}. \quad (2)$$

Here $\mathbf{A} \in \mathbb{R}^{p \times p}$ is a finite-dimensional linear approximation of the Koopman operator $\mathcal{K}$, determined by solving the following *least squares error minimization problem*

$$\min_{\mathbf{A} \in \mathbb{R}^{p \times p}} \|\mathbf{Y}^+ - A\mathbf{Y}\|_{\mathrm{F}}^2. \quad (3)$$

An exact solution to problem (3) is estimated by $\mathbf{A} = \mathbf{Y}^+\mathbf{Y}^\dagger \in \mathbb{R}^{p \times p}$, where the symbol "$\dagger$" is the Moore-Penrose pseudoinverse. Generally, we first project onto a low-dimensional subspace to reconstruct the dominant nonzero eigenvalues and eigenvectors of the matrix $\mathbf{A}$.

The numerical method for such exact (DMD)[1] proposed by Tu *et al.* [3], utilizes the singular value decomposition (SVD) with a truncated rank r such that $\mathbf{Y} = \mathbf{U}\mathbf{\Sigma}\mathbf{V}^*$, where $\mathbf{U} \in \mathbb{R}^{p \times r}$, $\mathbf{\Sigma} \in \mathbb{R}^{r \times r}$, $\mathbf{V} \in \mathbb{R}^{N \times r}$. The columns of $\mathbf{U}$ and $\mathbf{V}$ are orthonormal and $\mathbf{\Sigma}$ is diagonal. We obtain $\mathbf{A} = \mathbf{Y}\mathbf{V}\mathbf{\Sigma}^{-1}\mathbf{U}^*$. By computing $\tilde{\mathbf{A}} = \mathbf{U}^*\mathbf{Y}\mathbf{V}\mathbf{\Sigma}^{-1} \in \mathbb{R}^{r \times r}$, it yields the eigen-decomposition $\tilde{\mathbf{A}}\mathbf{W} = \mathbf{W}\mathbf{\Lambda}$. Finally, we have $\mathbf{A} = \mathbf{\Phi}\mathbf{\Lambda}\mathbf{\Phi}^{-1}$ and thus

$$\mathbf{A}(\mathbf{Y}\mathbf{V}\mathbf{\Sigma}^{-1}\mathbf{W}) = (\mathbf{Y}\mathbf{V}\mathbf{\Sigma}^{-1}\mathbf{W})\mathbf{\Lambda} := \mathbf{\Phi}\mathbf{\Lambda}, \quad (4)$$

where the columns of $\mathbf{W}$ are eigenvectors and $\mathbf{\Lambda}$ is a diagonal matrix of the corresponding eigenvalues λ_i, $i = 1, \cdots, r$, and $\mathbf{\Phi}$ is called DMD modes [11, Chap. 1].

---

[1] Specifically, the linear model (2) of the dynamics can be reconstructed onto projected coordinates $\tilde{\mathbf{y}} = \mathbf{U}^*\mathbf{y}$, namely, $\tilde{\mathbf{y}}_{k+1} \approx \tilde{\mathbf{A}}\tilde{\mathbf{y}}_k$.

Therefore, we have a reduced-order approximation:

$$\mathbf{y}_k \approx \sum_{j=1}^r \phi_j \lambda_j^k b_j, \quad \Longrightarrow \quad \mathbf{Y} \approx \mathbf{\Phi}\mathbf{D}_\mathbf{b}\mathbf{\Xi}, \quad (5)$$

where $\mathbf{\Phi} \in \mathbb{C}^{p \times r}$ is the so-called *spatial modes*, $\mathbf{D}_\mathbf{b} \triangleq \mathrm{diag}(b_1, \ldots, b_r)$ is the *amplitudes* with diagonal form (resp., $\mathbf{b} \triangleq [b_1, \ldots, b_r]$ denotes its vector case), and $\mathbf{\Xi} \in \mathbb{C}^{r \times N}$ indicates the Vandermonde matrix consisting of the eigenvalues to record the *temporal dynamics*.

2.2. Method-II: Sparsity-Promoting DMD

According to the above (5), the DMD least-square error problem with ℓ_0 "norm" regularization is written as

$$\min_{\mathbf{b} \in \mathbb{C}^r} \|\mathbf{Y} - \mathbf{\Phi}\mathbf{D}_\mathbf{b}\mathbf{\Xi}\|_{\mathrm{F}}^2 + \gamma \sum_{i=1}^r \iota(b_i \neq 0). \quad (6)$$

Here $\iota(\cdot)$ is an indicator function that measures the level of sparsity by counting the number of non-zero elements, that is, 1 if $b_i \neq 0$ and 0 otherwise. A tunable parameter $\gamma \geq 0$ denotes the sparsity weight that makes the trade-off between the least-square error (i.e., accuracy) and the number of reduced amplitudes (i.e., model complexity). As is well known, the program (6) is a nonconvex optimization problem. However, it can be addressed using a convex surrogate, namely the ℓ_1-regularized formulation (7), which is commonly referred to as *sparsity-promoting* dynamic mode decomposition (SPDMD) [12].

Mathematically, SPDMD solves a *regularized least squares error minimization problem* of (6) as below

$$\mathcal{J}_\gamma(\mathbf{b}) \triangleq \min_\mathbf{b} \|\mathbf{Y} - \mathbf{\Phi}\mathbf{D}_\mathbf{b}\mathbf{\Xi}\|_{\mathrm{F}}^2 + \gamma \sum_{i=1}^r |b_i|, \quad (7)$$

where $\sum_{i=1}^r |b_i|$ indicates the sum of the absolute values of DMD amplitudes, or equivalently the ℓ_1 norm $\|\mathbf{b}\|_1$. Clearly, if $\gamma \to 0$, the program (6) or (7) reduces to the computation (3). Problem (7) is a convex optimization.

The derivation $\|\mathbf{Y} - \mathbf{\Phi}\mathbf{D}_\mathbf{b}\mathbf{\Xi}\|_{\mathrm{F}}^2$ of the sparse optimal amplitudes $\mathbf{b}^\star$, is obtained from the SPDMD algorithm, in fraction of normalized original data $\|\mathbf{Y}\|_{\mathrm{F}}^2$, then we take the performance loss $\Pi\%$ into account, evaluated by

$$\Pi\% := 100\sqrt{\frac{\mathcal{J}(\mathbf{b}^\star)}{\mathcal{J}(0)}} = \frac{\|\mathbf{Y} - \mathbf{\Phi}\mathbf{D}_\mathbf{b}\mathbf{\Xi}\|_{\mathrm{F}}}{\|\mathbf{Y}\|_{\mathrm{F}}} \times 100. \quad (8)$$

Solving (7) or (6) yields a sparse amplitude vector $\mathbf{b}^\star$ with cardinality $\mathrm{card}(\mathbf{b}^\star(\gamma)) = s$, indicating s nonzero dominant modes ordered by $|b_i|$, $i = 1, \ldots, s$. Letting $m \triangleq \min\{s, r\}$, where r is the SVD truncation rank in (4), we can obtain a low-dimensional system model using only the selected m modes.

3. APPLICATIONS: SEA SURFACE TEMPERATURE DATA FIELD

In this section, we apply KMD and SPDMD to real-world data-driven climate dynamics to extract the dominant Koopman modes that characterize Pacific SST variability and reveal underlying climate patterns.
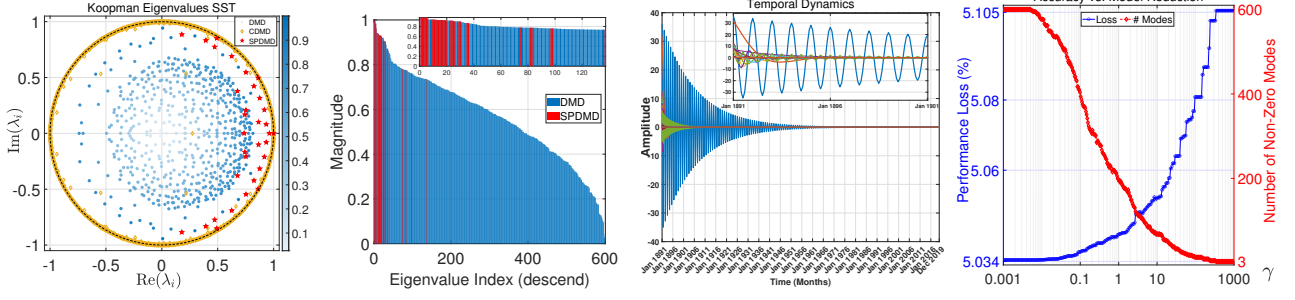
Fig. 1: (left) The distribution of spectrum of Pacific monthly SST with all 600 eigenvalues obtained via DMD (blue), CDMD (yellow), and the 33 dominant eigenvalues identified by SPDMD (red); (mid-I) the magnitude of the eigenvalues; (mid-II) the time evolution of temporal dynamics by the selected modes; (right) the accuracy versus the model complexity.

3.1. Data Source: Long-Term SST Data

In this context, the (long-term) time-series dataset are obtained from monthly SST over Niño-3 index[2], taking only sea mask into account (without land data information); For more details, we refer to see the available data source[3] (see also [22]). Besides, the chosen tropical region belt between the 5°N and 5°S in the direction of latitude and extends from 150°W to 90°W in the direction of longitude. More specifically, the dataset consists of monthly SST fields spanning from January 1891 to December 2019 for a total of 129 years and corresponding long-term 1548 months. In other words, we collect the monthly SST data by stacking each snapshot into a (long) vector field as a column, then the rolling horizon data is

$$\{\mathbf{y}_0, \mathbf{y}_1, \ldots, \mathbf{y}_N\}, \qquad (9)$$

where the vector $\mathbf{y}_k \in \mathbb{R}^{600 \times 1}$ of spatial length $p = 600$ denotes the system at different time steps $k = 0, 1, \ldots, 1547$ (that is, $N = 1548$). Let $\mathbf{Y}^+$ be the one time delay-embedding (or time-shifted) copies of the zero-lag time data matrix of $\mathbf{Y}$ in (1). Each data point contains monthly SST data measured on a snapshot size of $10 \times 60 = 600$ grids, with 60 grid points along the longitude and 10 grid points along the latitude. Therefore, in general each grid point implies a degree of the freedom, indicating a high dimensional climate system problem.

Table 1: The first 11 key modes ordered by amplitudes.

Mode i	Amps $\|b_i\|$	Norm $\|\lambda_i\|$	e-folding time $-1/|\mathrm{Re}(\log \lambda_i)|$	Period (mths) $2\pi/\mathrm{Im}(\log \lambda_i)$
1 (45)	641.79	1.00	Inf	Inf
3 (41)	36.14	0.99	186.97	12.00
5 (66)	31.94	0.94	15.48	73.15
7 (60)	12.64	0.93	13.03	13.26
9 (52)	12.52	0.93	13.76	10.01
11 (62)	10.69	0.93	13.92	18.12
13 (63)	8.80	0.94	16.47	27.84
15 (72)	8.39	0.87	7.24	53.98
17 (248)	8.33	0.78	4.05	23.29
19 (294)	7.91	0.76	3.66	28.37
21 (145)	7.46	0.78	3.94	12.33

3.2. Experiment 1: Monthly SST Data Field

We first explore climate dynamics, focusing on high-resolution (i.e., one data point per month) intraseasonal

[2] https://psl.noaa.gov/gcos_wgsp/Timeseries/Nino3
[3] The animation showing the time evolution of monthly SST is available.

SST variability by studying Koopman modes and their month-to-month changes. This variability plays a key role in simulating tropical phenomena, such as MJO, which is characterized by a phase evolution over a 30–90 day period [13]. The spectral distribution of the linear operator on monthly SST is shown in Fig. 1 (left). In this figure, the "blue dots" represent eigenvalues estimated using the DMD algorithm described in (4), the "yellow diamonds" correspond to the companion-based DMD (CDMD) method [8], and the "red stars" denote eigenvalues obtained through SPDMD [12] as formulated in (7). It is worth noting that for such a flat data matrix, the CDMD is particularly useful for studying oscillatory behavior (e.g., MJO event), as the spectrum of the companion matrix is predominantly distributed along the unit circle. In contrast, both standard DMD and SPDMD tend to place the eigenvalues strictly inside the unit circle. Nonetheless, all three methods (DMD, CDMD, and SPDMD) consistently indicate that the modes are stable, as verified by Koopman eigenvalues with magnitude or absolute value less than one in Fig. 1 (mid-I), implying that the monthly SST data-embedded climate system enjoys a *stationary state*. Additionally, Table 1 presents the first 11 dominant Koopman modes, ordered by the magnitude of their amplitudes.

By promoting sparsity on the amplitudes, it consists entire spectrum of $r = 600$ modes, reducing it to a smaller number of $m = 33$ modes. This reduction is significant as it enables us to capture the leading modes of the high-dimensional climate system, allowing for a more focused analysis through a low-dimensional system representation. Fig. 1 (mid-II) illustrates the time evolution of the real part of the temporal dynamics governed by $\mathrm{Re}(\lambda_j^t b_j)$, corresponding to the first 17 leading modes (conjugate pairs) ordered by the magnitude of their amplitudes $|b_j|$. In the case of complex conjugate pairs, only one spatiotemporal mode is shown. These dynamics are governed by the Koopman eigenfunctions, whose temporal evolution eventually decays to steady-state in zero.

Fig. 1 (right) illustrates the trade-off between accuracy (evaluated by performance loss) and model complexity (measured by the number of non-zero modes) as analyzed via SPDMD in the monthly SST. By tuning the sparsity weight $\gamma \in [0.001, 1000]$ with 350 grids, we observe that
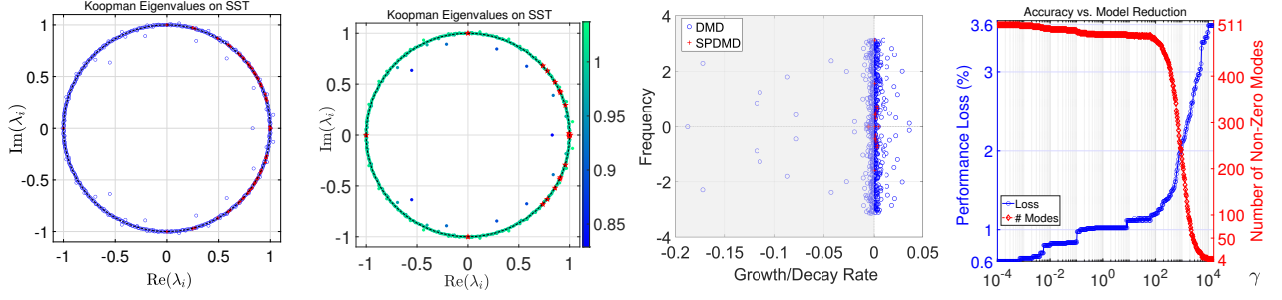
Fig. 2: (left) Koopman eigenvalues for the seasonal cycle of the SST data field, including all 515 modes and the selected 57 eigenvalues; (mid-I) The 19 eigenvalues selected by SPDMD; (mid-II) the growth or decay rate versus the frequency; (right) the balance between accuracy and model reduction under different sparsity weights $\gamma \in [0.0001, 16000]$.
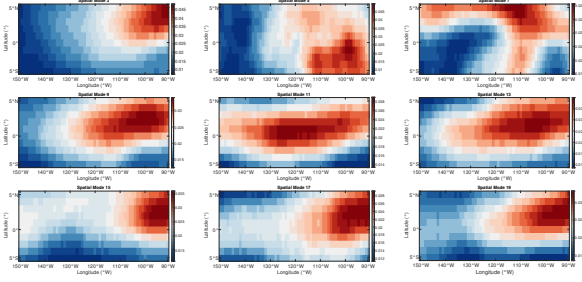

Fig. 3: Spatial Modes for seasonal cycle of SST data.

Table 3: The first 10 key modes ordered by amplitudes.

Mode	Amps	Norm	Eigenvalue	Period (season)
i	$\|b_i\|$	$\|\lambda_i\|$	λ_i	$2\pi/\mathrm{Im}(\log \lambda_i)$
1 (412)	1058.52	1.00	1.0003 + 0.0000i	Inf
3 (445)	24.47	1.00	0.0005 − 1.0003i	4.00
5 (505)	3.19	1.00	-1.0004 + 0.0000i	2.00
7 (417)	1.73	0.99	0.9946 + 0.0153i	407.19
9 (180)	1.49	1.00	0.8563 − 0.5203i	11.51
11 (242)	1.23	1.00	0.9035 − 0.4320i	14.09
13 (7)	0.36	1.00	0.7361 + 0.6813i	8.41
15 (335)	0.36	1.00	0.9576 + 0.2934i	21.31
17 (20)	0.29	1.00	0.7803 − 0.6307i	9.24
19 (264)	0.21	1.00	0.9088 − 0.4180i	14.57

the deviation in least squares error is not negligible, with a loss of $\Pi\% = 5.034\%$. Also, the number of modes gradually decreases from 600 to 3 as the weight increases.

Table 2: Model reduction with the number of modes, the cost, and the performance loss in seasonal cycle of SST.

Weight γ	Modes #i	Cost $\mathcal{J}(\mathbf{b}^\star)$	Loss $\Pi\%$
0.0001	511	2.2308×10^4	0.6010
0.0105	501	1.1602×10^5	0.8277
0.5503	490	1.8414×10^5	1.0224
8.5573	488	2.2331×10^5	1.1172
100.24	478	2.3250×10^5	1.1983
691.05	303	3.4864×10^5	1.8255
1714.3	107	4.7381×10^5	2.3815
4948.2	19	7.7276×10^5	3.0350
5757.2	9	8.6025×10^5	3.3761
16000	4	1.6447×10^6	3.5880

3.3. Experiment 2: Seasonal Cycle of SST Data Field

We now discuss the seasonal cycle of SST data field by first organizing the 3-month data matrices into a vector field. Thus, the snapshot spans the spatial points, encompassing a medium resolution time scale (one data point per season, typically averaging 3 months of grid data), and forms a high-dimensional vector $\mathbf{y}_k \in \mathbb{R}^{1800 \times 1}$ with $p = 1,800$. In this case, the data for each quarter is then aggregated by stacking the spatial points from each season into a single vector. Consequently, the number of snapshots becomes to $N = 515$, resulting in a *tall-and-skinny* data matrix $\mathbf{Y} \in \mathbb{R}^{1800 \times 515}$. This data matrix $\mathbf{Y}$ is transformed into four seasonal cycles, helping to eliminate seasonal variations, such as changes in temperature and precipitation factors. In general, quarterly SST data

is good for capturing the ENSO [17], as it concerns on a seasonal-to-interannual timescale, with its impacts often becoming most apparent over several months to a year.
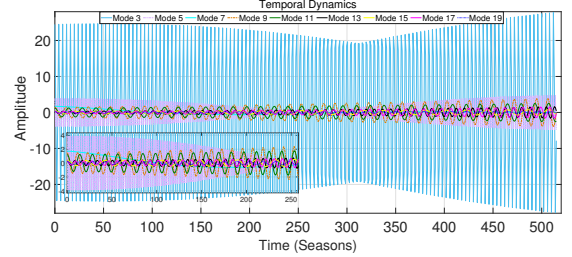

Fig. 4: The real part of selected 9 temporal modes show the oscillations with periodic behavior in seasonal SST.

By virtue of DMD and SPDMD, Fig. 2 (left and mid-I) showed the distribution of Koopman eigenvalues on seasonal cycle of (or quarterly) SST data case, exhibiting a distinct "ring" structure. This sharp contrasts with the monthly SST case shown on the left of Fig. 1, where most eigenvalues lie within the unit circle, while the ring sharp is also similar to that observed in the CDMD in Subsection 3.2. Fig. 2 (mid-II) plots the growth or decay rate $\mathrm{Re}(\log \lambda_i)$ against the frequency $\mathrm{Im}(\log \lambda_i)$ for the 19 modes. Furthermore, Fig. 2 (right) depicts the trade-off between the accuracy and model-reduction of modes, governed by the range of γ values, with $\gamma_{\min} = 0.0001$ and $\gamma_{\max} = 16000$, using 500 grids, where the function $\mathbf{b}(\gamma)$ reduces the number of modes from 511 to only 4, and the performance loss function $\Pi\%$ varies from 0.6% to 3.58%. On the other hand, the sparsity level of the amplitudes achieved by the solution $\mathbf{b}^\star$ depends on the

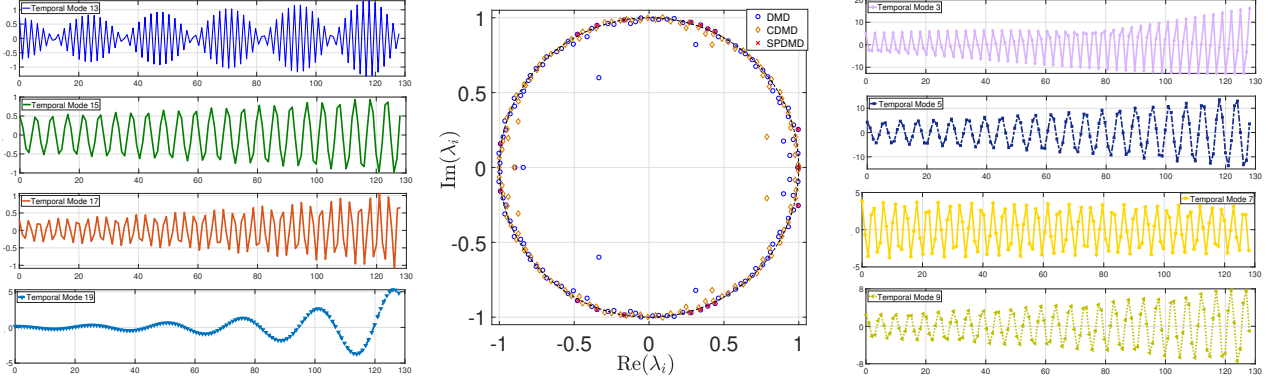Fig. 5: Spectrum distributions of approximated Koopman matrix A w.r.t. annual cycle of SST dataset through DMD ($\circ$), CDMD ($\diamond$) and SPDMD ($\times$), respectively. Here the first mode is ignored since it takes "Inf" with nearly zero imaginary part (non-oscillation) with eigenvalues $\lambda_1 \approx 1.000 + 0000\mathrm{i}$. The rest plots show the extracted modes via SPDMD.

weight parameter $\gamma \geq 0$. Hence, $\mathbf{b}(\gamma)$ quantifies the sparsity of the solution, giving a measure of whether a new γ results in a sparser solution or not. The interplay between $\mathbf{b}$ and γ is formalized through the concept of appropriateness: we say that the weight γ is appropriate for the idea amplitude $\mathbf{b}$ if a user-specified satisfaction condition is fulfilled, ensuring that the corresponding loss $\Pi\%$ remains acceptable level even with a small number of the captured dominant modes.

SPDMD is applied to determine the number of Koopman modes, where the extracted Koopman modes, in terms of their spatial structure, are shown in Fig. 3. The identified 9 leading modes in the seasonal cycle of the SST data are visualized using the magnitude of the real part of Koopman modes $|\phi_i|$ for $i = 3, 5, \dots, 19$. Meanwhile, Fig. 4 illustrates the real part of the temporal dynamics over seasonal time units. With an eye toward model reduction, SPDMD captures the dominant modes associated with those (quasi) periodic behavior (e.g., see Table 3) and can also be used for model reduction near periodic Koopman eigenfunctions, simplifying the system's behavior from a large number of degrees of freedom to a low-dimensional representation while preserving its essential dynamics [6].

3.4. Experiment 3: Annual Cycle of SST Data Field

Finally, we study the experiment on the annual cycle of SST data field. The analysis focuses on short-term climate dynamics with yearly snapshots $N = 128$ and low resolution (i.e., a data point per year with $p = 7200$), leading to a data matrix $\mathbf{Y} \in \mathbb{R}^{7200 \times 128}$. Similar to the trials above, the distributions of the Koopman eigenvalues obtained using DMD, CDMD, and SPDMD are labeled with different markers and displayed in Fig. 5. Clearly, SPDMD effectively captures the dominant modes with large norm of amplitudes. Along with the information on eigenvalues and amplitudes, Fig. 5 gives the time evolution of temporal dynamics from the observed annually SST data. Fig. 6 provides the trade-off between the least-squares approximation error and the number of reduced modes, where the sparsity weight varies as $\gamma \in [1, 10^4]$ across 400 grid points. Obviously, a

dramatic jump happens in the number of modes, decreasing from 26 to 21, while the loss increases from 2.7533 to 3.5379. This transition corresponds to a change in the sparsity weight from 1.6907×10^3 to 1.8543×10^3. Fig. 7
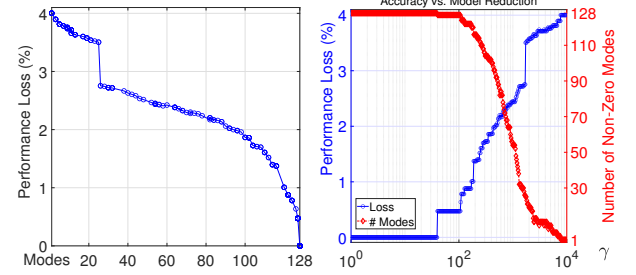

Fig. 6: Loss vs. nonzero modes in annual cycle of SST.

shows the element-wise of absolute value of the spatial modes on annual cycle case of SST data.

4. CONCLUSIONS

This paper extracted the dominant spatial and temporal modes of climate dynamics from SST data fields using KMD and SPDMD. The leading modes captured reveal the variability of climate dynamics across different cycles (e.g., monthly, seasonal, and annual) of the SST data. By tuning the sparsity weights, we achieved a balance between accuracy and model complexity. Future work will focus on exploring climate modes through data assimilation or ensemble methods, incorporating a broader range of SST fields and land data.

ACKNOWLEDGMENT

REFERENCES

[1] J. Marshall and R. A. Plumb, *Atmosphere, ocean and climate dynamics: an introductory text*. Academic Press, 1961.

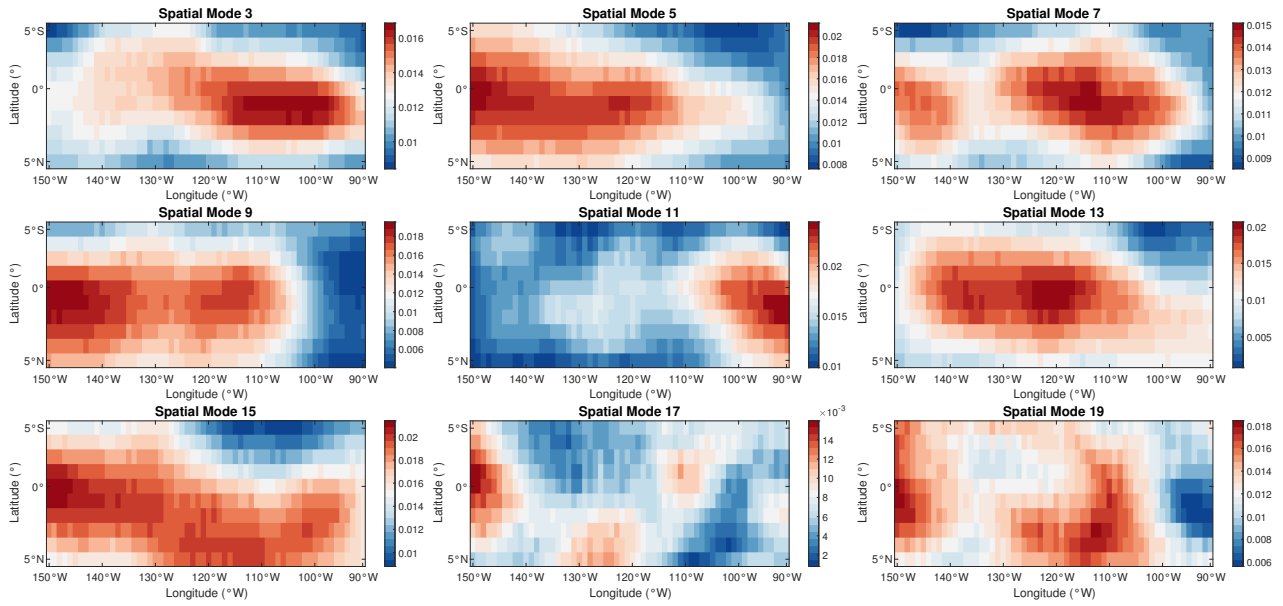[2] M. Ghil, M. D. Chekroun, and E. Simonnet, "Climate dynamics and fluid mechanics: Natural vari-

Fig. 7: The magnitude of the spatial modes for annual cycle of SST.

ability and related uncertainties," *Physica D*, vol. 237, no. 14-17, pp. 2111–2126, 2008.

[3] J. H. Tu, C. W. Rowley, D. M. Luchtenburg, S. L. Brunton, and J. N. Kutz, "On dynamic mode decomposition: Theory and applications," *J. Comput. Dyn.*, vol. 1, no. 2, pp. 391–421, 2014.

[4] O. T. Schmidt, G. Mengaldo, G. Balsamo, and N. P. Wedi, "Spectral empirical orthogonal function analysis of weather and climate data," *Mon. Weather Rev.*, vol. 147, no. 8, pp. 2979–2995, 2019.

[5] B. O. Koopman, "Hamiltonian systems and transformation in Hilbert space," *Proc. Natl. Acad. Sci.*, vol. 17, no. 5, pp. 315–318, 1931.

[6] I. Mezić, "Spectral properties of dynamical systems, model reduction and decompositions," *Nonlin. Dyna*, vol. 41, pp. 309–325, 2005.

[7] A. Mauroy, I. Mezic, and Y. Susuki, *Koopman operator in systems and control*. Springer, 2020.

[8] C. W. Rowley, I. Mezić, S. Bagheri, P. Schlatter, and D. S. Henningson, "Spectral analysis of nonlinear flows," *J. Fluid Mech.*, vol. 641, pp. 115–127, 2009.

[9] I. Mezić, "Analysis of fluid flows via spectral properties of the Koopman operator," *Ann. Rev. Fluid Mech.*, vol. 45, no. 1, pp. 357–378, 2013.

[10] Y. Susuki and I. Mezic, "Nonlinear Koopman modes and coherency identification of coupled swing dynamics," *IEEE Trans. Power Sys.*, vol. 26, no. 4, pp. 1894–1904, 2011.

[11] J. N. Kutz, S. L. Brunton, B. W. Brunton, and J. L. Proctor, *Dynamic mode decomposition: Data-driven modeling of complex systems*. SIAM, 2016.

[12] M. R. Jovanović, P. J. Schmid, and J. W. Nichols, "Sparsity-promoting dynamic mode decomposition," *Phys. Fluids*, vol. 26, no. 2, 2014.

[13] B. R. Lintner, D. Giannakis, M. Pike, and J. Slawinska, "Identification of the Madden–Julian oscilla-tion with data-driven Koopman spectral analysis," *Geo. Res. Lett.*, vol. 50, no. 10, pp. 1–10, 2023.

[14] R. Alexander, Z. Zhao, E. Székely, and D. Giannakis, "Kernel analog forecasting of tropical intraseasonal oscillations," *J. Atmos. Sci.*, vol. 74, no. 4, pp. 1321–1342, 2017.

[15] D. Giannakis, J. Slawinska, and Z. Zhao, "Spatiotemporal feature extraction with data-driven Koopman operators," in *PRML*, 2015, pp. 103–115.

[16] X. Wang, J. Slawinska, and D. Giannakis, "Extended-range statistical ENSO prediction through operator-theoretic techniques for nonlinear dynamics," *Sci. Rep.*, vol. 10, no. 1, p. 2636, 2020.

[17] G. Froyland, D. Giannakis, B. R. Lintner, M. Pike, and J. Slawinska, "Spectral analysis of climate dynamics with operator-theoretic approaches," *Nature Comm.*, vol. 12, no. 1, p. 6570, 2021.

[18] A. Navarra, J. Tribbia, and S. Klus, "Estimation of Koopman transfer operators for the equatorial pacific SST," *J. Atmos. Sci.*, vol. 78, no. 4, pp. 1227–1244, 2021.

[19] A. Navarra, J. Tribbia, S. Klus, and P. Lorenzo-Sánchez, "Variability of SST through Koopman modes," *J. Clim.*, vol. 37, no. 16, pp. 4095–4114, 2024.

[20] J. Hogg, M. Fonoberova, and I. Mezić, "Exponentially decaying modes and long-term prediction of sea ice concentration using Koopman mode decomposition," *Sci. Rep.*, vol. 10, no. 1, p. 16313, 2020.

[21] M. J. Colbrook and A. Townsend, "Rigorous data-driven computation of spectral properties of Koopman operators for dynamical systems," *Comm. Pure Appl. Math.*, vol. 77, no. 1, pp. 221–283, 2024.

[22] Z. Zhang, Y. Susuki, and A. Okazaki, "Sparsity-promoting dynamic mode decomposition applied to sea surface temperature fields," *arXiv preprint arXiv:2507.05711v2*, 2025.